ADVANCED FUNCTIONAL MATERIALS
www.afm-journal.de

Trimetallic Mn-Fe-Ni Oxide Nanoparticles Supported on Multi-Walled Carbon Nanotubes as High-Performance Bifunctional ORR/OER Electrocatalyst in Alkaline Media

Dulce M. Morales, Mariya A. Kazakova, Stefan Dieckhöfer, Alexander G. Selyutin, Georgiy V. Golubtsov, Wolfgang Schuhmann, and Justus Masa**

Discovering precious metal-free electrocatalysts exhibiting high activity and stability toward both the oxygen reduction (ORR) and the oxygen evolution (OER) reactions remains one of the main challenges for the development of reversible oxygen electrodes in rechargeable metal–air batteries and reversible electrolyzer/fuel cell systems. Herein, a highly active OER catalyst, $Fe_{0.3}Ni_{0.7}O_X$ supported on oxygen-functionalized multi-walled carbon nanotubes, is substantially activated into a bifunctional ORR/OER catalyst by means of additional incorporation of MnO_X. The carbon nanotube-supported trimetallic (Mn-Ni-Fe) oxide catalyst achieves remarkably low ORR and OER overpotentials with a low reversible ORR/OER overvoltage of only 0.73 V, as well as selective reduction of O_2 predominantly to OH^-. It is shown by means of rotating disk electrode and rotating ring disk electrode voltammetry that the combination of earth-abundant transition metal oxides leads to strong synergistic interactions modulating catalytic activity. The applicability of the prepared catalyst for reversible ORR/OER electrocatalysis is evaluated by means of a four-electrode configuration cell assembly comprising an integrated two-layer bifunctional ORR/OER electrode system with the individual layers dedicated for the ORR and the OER to prevent deactivation of the ORR activity as commonly observed in single-layer bifunctional ORR/OER electrodes after OER polarization.

1. Introduction

Earth-abundant transition metal oxides (MO_X), including oxides of nickel, cobalt, manganese, and iron, are attractive for electrocatalytic applications due to their wide availability, rich structural diversity, and comparatively high resistance to corrosion in alkaline media.[1] MO_X thus represent an appealing alternative to the well-established noble metal-based electrocatalysts for the oxygen reduction (ORR)[2] and the oxygen evolution (OER)[3] reactions. However, a major drawback of MO_X is their generally poor electrical conductivity, which impedes electron transfer processes that are essential for driving electrochemical reactions.[4] To circumvent the high electrical resistances of MO_X, conductive additives such as carbon materials are often used, enhancing the electrical conductivity as well as the surface area.[2,5] Their properties can be further modified, e.g., through heteroatom functionalization,[6] or by engineering of defects as potential anchoring sites for active nanoparticles.[7] Thus, a wide variety of MO_X/C-type materials has been proposed as catalysts for OER,[7,8] ORR,[9] and for reversible ORR/OER.[10–12] Materials used for the latter are commonly known as bifunctional oxygen electrodes (BOEs), finding application in electrochemical devices which require the reversible conversion of water into oxygen and vice versa, such as rechargeable metal–air batteries and reversible fuel cells.[13]

In a previous work, we showed a method for preparing ORR/OER active composites consisting of transition metal oxide nanoparticles supported on oxygen-functionalized multi-walled carbon nanotubes (MWCNTs-Ox).[14] The method involved growth and functionalization of MWCNTs to obtain MWCNTs-Ox with an average outer diameter of 8 to 10 nm, a Brunauer–Emmett–Teller (BET) surface area of about 300 $m^2\ g^{-1}$, and about 2.4 carboxylic acid functional groups per nm^2. MWCNTs-Ox were thereafter modified by wet impregnation with aqueous iron and cobalt nitrate solutions, and subsequently annealed at 350 °C to form metal oxide phases. The proposed method proved to be effective for controlled synthesis of a series of $Fe_nCo_{1-n}O_X$/MWCNTs-Ox-type catalysts that exhibited high activity for both the ORR and the OER. It was shown through

Dr. D. M. Morales, S. Dieckhöfer, Prof. W. Schuhmann, Dr. J. Masa
Analytical Chemistry – Center for Electrochemical Sciences (CES)
Faculty of Chemistry and Biochemistry
Ruhr University Bochum
Universitätsstr. 150, Bochum 44780, Germany
E-mail: wolfgang.schuhmann@rub.de; justus.masa@rub.de
Dr. M. A. Kazakova, A. G. Selyutin, G. V. Golubtsov
Boreskov Institute of Catalysis
SB RAS
Lavrentieva 5, Novosibirsk 630090, Russia
Dr. M. A. Kazakova
Novosibirsk State University
Pirogova 2, Novosibirsk 630090, Russia
The ORCID identification number(s) for the author(s) of this article can be found under https://doi.org/10.1002/adfm.201905992.

DOI: 10.1002/adfm.201905992

in-depth structural characterization that the size and location (inside or outside the MWCNTs) of the metal oxide nanoparticles varied with the Fe/Co ratio. The lowest ORR/OER overpotentials were observed for samples with Fe/Co ratios close to 1, due to optimal particle size distribution and location, as well as an improved film conductivity and active site density.[14] In a follow-up work, we employed a similar synthesis route to prepare trimetallic systems containing oxides of iron, nickel, and cobalt,[15] where the electrocatalytic performance of cobalt and nickel-based oxides toward the ORR and the OER, respectively, was significantly boosted upon the addition of iron due to synergistic interactions. We demonstrated that $Fe_nNi_nCo_{1-2n}O_X$/MWCNTs-Ox (n = 0.2–0.4) did not only exhibit enhanced bifunctional ORR/OER activity, but also improved stability and ORR selectivity compared to the bi- and monometallic analogs.[15]

Among all the samples investigated in our aforementioned works,[14,15] the bimetallic composite $Fe_{0.3}Ni_{0.7}O_X$/MWCNTs-Ox exhibited the lowest overpotential toward the OER, attaining a current density of 10 mA cm^{-2} at a potential of 1.55 V versus reversible hydrogen electrode (RHE). However, the same composite exhibited rather poor ORR activity. It is a common observation that highly active OER electrocatalysts require rather large overpotentials to drive the ORR, or vice versa. For that reason, a typical design approach of BOEs involves integrating individual high-performance ORR and OER catalysts into a hybrid material, where one component catalyzes the OER while the other catalyzes the ORR. For instance, the activation of perovskite-based OER catalysts for ORR was achieved by heat-treating the perovskite in the presence of iron phthalocyanine and nitrogen-doped carbon to incorporate ORR-active FeN_X/C groups.[16] A highly active bifunctional composite consisting of $NiFeO_X$ (OER active) and CoN_Y/C (ORR active) moieties, prepared by calcination of NiFe layered double hydroxide intercalated with cobalt phthalocyanine was proposed,[17] as well as a procedure for the thermal decomposition of N-rich metal macrocyclic compounds that leads to the formation of MO_X and MN_Y/C groups, which are active sites for the OER and ORR, respectively.[10,18]

Herein, we report the incorporation of manganese oxide into $Fe_{0.3}Ni_{0.7}O_X$/MWCNTs-Ox as a strategy to enhance the ORR activity of the composite, taking advantage of the promising ORR activity of manganese oxide-based materials for selective reduction of O_2 to OH^-.[19] We investigate systematically the bifunctional activity toward the ORR and the OER of the prepared catalysts as a function of the metal composition, evaluating the applicability of the obtained materials as BOEs. Additionally, we investigate the long-term performance of the optimized catalyst by subjecting it alternately to cathodic (ORR) and anodic (OER) polarization in a three-electrode setup, as well as in a four-electrode setup proposing an integrated two-layer bifunctional ORR/OER electrode system with the individual layers dedicated exclusively either for the ORR or the OER to prevent deactivation of the ORR activity as commonly observed in single-layer bifunctional ORR/OER electrodes after polarization to the high anodic OER potentials.

2. Results and Discussion

The MO_X/MWCNTS-Ox catalysts were prepared following a previously described synthesis route.[14,15] This synthesis procedure offers a number of advantages, including the possibility for controlled preparation of a large number of MO_X/MWCNTs-Ox-type samples, containing one or more earth-abundant transition metals at different metal loadings and ratios, by merely varying the composition of the precursor solutions. Moreover, the electrical resistances inherent to metal oxides are overcome by connecting the MO_X-nanoparticles with MWCNTs-Ox, which does not provide only high electrical conductivity but also a high degree of nanoparticle dispersion and hence high surface area (275 m^2 g^{-1}). The grown MWCNTs possess narrow size distributions, which ensures samples of uniform structural properties. These advantages allowed us to conduct an in-depth investigation of the ORR/OER activity in correlation with the structure and composition of the prepared samples.

In our previous studies, the bimetallic catalyst $Fe_{0.3}Ni_{0.7}O_X$/MWCNTS-Ox was identified as a promising OER catalyst, achieving a current density of 10 mA cm^{-2} at a potential of as low as 1.55 V versus RHE.[15] This value is comparable to the benchmark OER-performance of iron-containing nickel oxide-based OER catalysts reported in the literature, including $NiFeO_X$,[20] $NiFeB_X$,[21] and NiFe layered double hydroxide (LDH).[22] In the present work, we used $Fe_{0.3}Ni_{0.7}O_X$ as an OER-benchmark and incorporated MnO_X with a twofold aim: first, to activate the composite for the ORR, and second, to explore potential synergistic interactions among the three transition metals which could lead to enhanced ORR and OER performances. To achieve this, the synthesis was carried out as described before, adjusting the concentration of the precursors $Mn(NO_3)_2$, $Ni(NO_3)_2$, and $Fe(NO_3)_3$ to prepare MO_X/MWCNTs-type samples with a total metal loading of ≈14 wt% and nominal mass composition M = Mn_nFe_{1-n} (n = 0, 0.3, 0.5, 0.7, 1), Mn_nNi_{1-n} (n = 0, 0.3, 0.5, 0.7, 1), and $Mn_n(Fe_{0.3}Ni_{0.7})_{1-n}$ (n = 0.1, 0.2, 0.3, 0.4, 0.5, 0.6, 0.8). The composition of M in the prepared MO_X/MWCNTs-Ox samples was determined by X-ray fluorescence (XRF) analysis and the obtained results are summarized in Table S1 in the Supporting Information. The actual composition of the metals in the samples was found to be in good agreement with the nominal values. Furthermore, the specific surface area of the catalysts did not change substantially upon modification of MWCNTs-Ox with MO_X-nanoparticles (Table S2, Supporting Information).

The electrocatalytic activity of the prepared samples toward the ORR and the OER was investigated by linear sweep voltammetry at an electrode rotation of 1600 rpm. Electrochemical impedance spectroscopy (EIS) was used for determining the uncompensated solution resistance, observing resistances in the range from 49 to 55 Ω in all cases. **Figure 1**a,b shows the ohmic-drop compensated voltammograms recorded in the OER and ORR potential regions, respectively, obtained with the sample set $Mn_n(Fe_{0.3}Ni_{0.7})_{1-n}O_X$/MWCNTS-Ox. $Fe_{0.3}Ni_{0.7}O_X$ exhibited the lowest overpotential toward the OER. As the content of MnO_X in the composite increased (or the concentration of $Fe_{0.3}Ni_{0.7}O_X$ decreased), the OER overpotential increased. $Mn_{0.8}(Fe_{0.3}Ni_{0.7})_{0.2}O_X$ displayed considerable higher OER activity than MnO_X even with a $Fe_{0.3}Ni_{0.7}$ loading of less than 3 wt%. These observations strongly suggest that $Fe_{0.3}Ni_{0.7}O_X$ is indeed the actual OER active component, and that the incorporation of Mn apparently results in a dilution of the density of the OER active sites, thereby leading to a decline

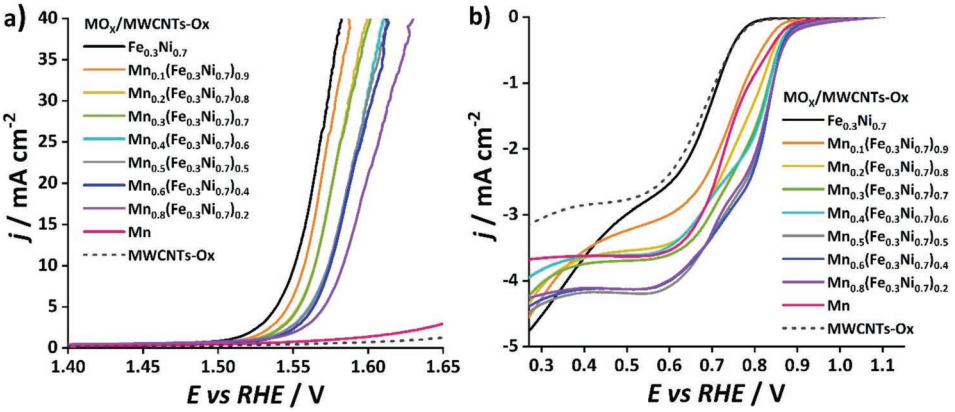

Figure 1. Linear sweep voltammograms of $Mn_n(Fe_{0.3}Ni_{0.7})_{1-n}O_X$/MWCNTs-Ox-type samples corresponding to the a) OER and b) ORR potential regions. The voltammograms were recorded in O_2-saturated 0.1 M KOH, at a scan rate of 5 mV s^{-1} and electrode rotation speed of 1600 rpm.

of the OER activity. On the contrary, a clear enhancement of the ORR activity was observed upon incorporation of MnO_X, with MnO_X:$Fe_{0.3}Ni_{0.7}O_X$ ratios between 1:1 and 4:1, exhibiting not only lower overpotentials but also larger diffusion limited-current density values than MnO_X or $Fe_{0.3}Ni_{0.7}O_X$ alone. Interestingly, these findings deviate from the observations made for the trimetallic NiFeMn LDH system.[23] There, doping of NiFe LDH with Mn led to the formation of a highly efficient OER catalyst, with an outstanding low OER overpotential of 262 mV at 10 mA cm^{-2}, which is about 80 mV lower than that of the best-performing $Mn_n(Fe_{0.3}Ni_{0.7})_{1-n}O_X$/MWCNTS-Ox catalysts presented here. However, the ORR overpotentials observed for the latter were substantially lower than for NiFeMn LDH, rendering them more suitable candidates for BOE applications.

To investigate the observed synergistic interactions between MnO_X and $Fe_{0.3}Ni_{0.7}O_X$ further, samples with compositions of Mn, Mn_nFe_{1-n}, and Mn_nNi_{1-n} were prepared and their ORR/OER activities were evaluated by linear sweep voltammetry (Figure S1, Supporting Information). The activity descriptors E_{OER}, E_{ORR}, corresponding to the potentials at which current densities of +10 (OER) and −1 mA cm^{-2} (ORR) were attained, respectively, were determined for each investigated sample to establish a relationship between composition and electrocatalytic activity. The difference between the two descriptors ($\Delta E = E_{OER} - E_{ORR}$) was used to assess the applicability of the catalysts as bifunctional oxygen electrodes. Data corresponding to the unmodified MWCNTs-Ox, the monometallic FeO_X and NiO_X, and the bimetallic set $Fe_nNi_{1-n}O_X$ were reported in our previous works.[14,15] The E_{OER}, E_{ORR}, and ΔE values obtained are summarized in Table S3 in the Supporting Information and represented graphically in **Figure 2** as a function of the metal composition.

As shown in Figure 2 (top row), catalysts containing a large amount of $Fe_nNi_{1-n}O_X$ exhibited the lowest E_{OER} values (1.55–1.57 V vs RHE), translating into higher OER activity. As it was mentioned before, the incorporation of Mn does not lead to a decrease of E_{OER}. On the other hand, the bimetallic systems Mn_nFe_{1-n} clearly display synergistic effects beneficial for the ORR as the three samples from the set outperformed the monometallic FeO_X and MnO_X samples. Therefore, although their contribution might be difficult to establish definitively, synergistic interactions occurring between FeO_X and MnO_X cannot be excluded. Regarding the ORR (Figure 2, middle row), Mn-containing samples delivered larger E_{ORR} values (lower overpotentials) than those where Mn was absent. Additionally, bimetallic samples with the compositions Mn_nFe_{1-n} and Mn_nNi_{1-n} exhibited considerable enhancement of activity compared to any of the monometallic composites. The best performing ORR catalysts were those of the sets $Mn_n(Fe_{0.3}Ni_{0.7})_{1-n}O_X$, $Mn_nFe_{1-n}O_X$, and $Mn_nNi_{1-n}O_X$, with $n \geq 0.5$, achieving E_{ORR} values in the range from 0.82 to 0.84 V versus RHE.

The bifunctional parameter ΔE is shown for each sample in Figure 2 (bottom row). The benchmark composite $Fe_{0.3}Ni_{0.7}O_X$ exhibited a ΔE value of 0.83 V. Incorporation of MnO_X resulted in a clear decrease of ΔE values (90–100 mV) in the case of the trimetallic $Mn_n(Fe_{0.3}Ni_{0.7})_{1-n}O_X$ composites with n between 0.2 and 0.8, outperforming not only all the other samples prepared for this work, but also all those from our previous reports.[14,15] Moreover, the best performing samples, namely, $Mn_{0.5}(Fe_{0.3}Ni_{0.7})_{0.5}O_X$ and $Mn_{0.6}(Fe_{0.3}Ni_{0.7})_{0.4}O_X$, achieved a ΔE as low as 0.73, or 0.76 V if ΔE is calculated as the difference between E_{OER} (at 10 mA cm^{-2}) and the ORR at half-way potential ($E_{1/2}$). To the best of our knowledge, the observed ΔE values are among the lowest reported to date in the literature for precious metal-free catalysts in alkaline media.[24,25] A list of highly active BOEs, including Co_3O_4/N-rGO (ΔE = 0.71 V),[26] Co_3O_4/CNTs (ΔE = 0.72 V),[27] Fe-N-C/NiFe LDH (ΔE = 0.75 V),[28] Fe/N-C (ΔE = 0.76 V),[11] and heat-treated Cs-MnO_X (ΔE = 0.78 V),[29] is shown in Table S4 in the Supporting Information for comparison. In addition to this, linear sweep voltammograms of commercial Pt (mixed with carbon black, 20 wt%), IrO_2, and RuO_2 (Sigma-Aldrich) were recorded and compared to $Mn_{0.5}(Fe_{0.3}Ni_{0.7})_{0.5}O_X$. As shown in Figure S2 in the Supporting Information, $Mn_{0.5}(Fe_{0.3}Ni_{0.7})_{0.5}O_X$ clearly outperformed the evaluated precious metal-based materials for bifunctional oxygen conversion applications in alkaline media.

Certainly, the low ΔE values observed are a consequence of both the high OER activity of $Fe_{0.3}Ni_{0.7}O_X$, which does not decline considerably when partially replacing $Fe_{0.3}Ni_{0.7}O_X$ with MnO_X, the intrinsic ORR activity of MnO_X, the strong synergistic contributions from the metal components, and the catalyst support. The observed low ORR overpotentials together

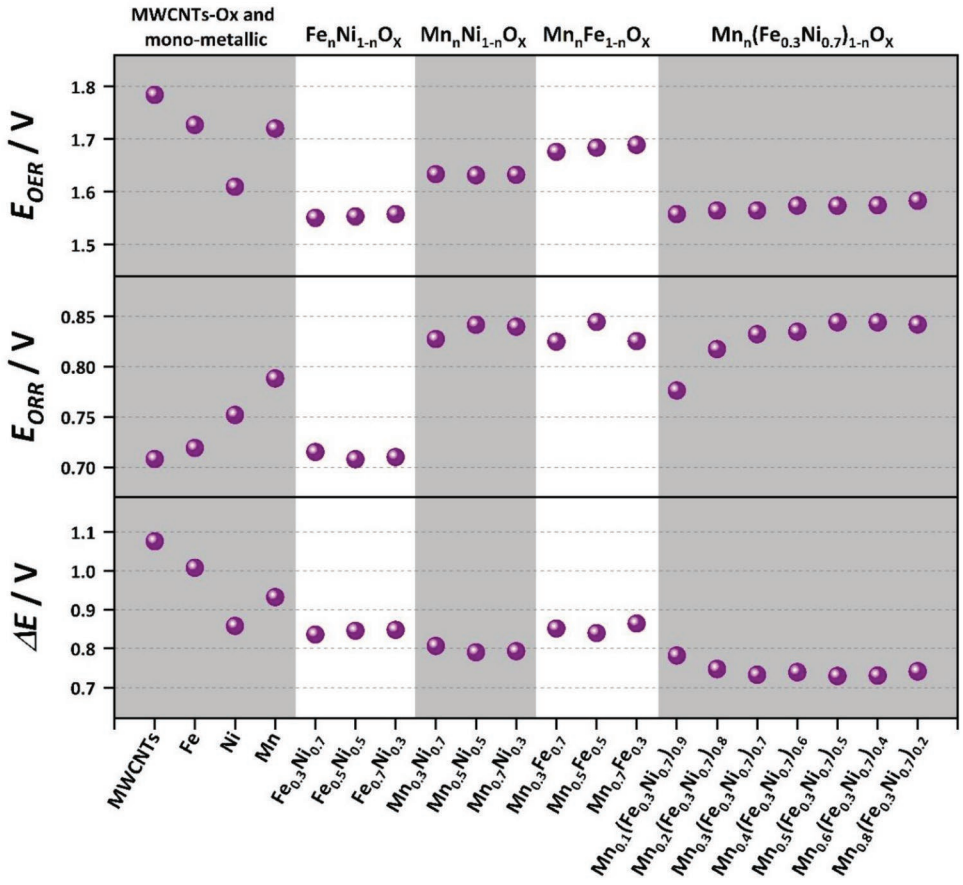

Figure 2. Activity descriptors E_{OER}, E_{ORR}, and ΔE of MO_X/MWCNTs-Ox-type catalysts as a function of the metal composition M, extracted from linear sweep voltammograms recorded in O_2-saturated 0.1 M KOH, at a scan rate of 5 mV s^{-1} and electrode rotation speed of 1600 rpm.

with enhanced diffusion limited currents could be an indication of the four-electron transfer reduction of O_2 being favored at the best performing samples, namely, $Mn_n(Fe_{0.3}Ni_{0.7})_{1-n}O_X$/MWCNTs-Ox with $n = 0.5$ and 0.6. To confirm this hypothesis, the ORR selectivity of the prepared composites was investigated by determining the yield of peroxide species ($\%HO_2^-$) during the ORR using rotating ring disk electrode (RRDE) voltammetry. The $\%HO_2^-$ resulting from each of the $Mn_n(Fe_{0.3}Ni_{0.7})_{1-n}O_X$/MWCNTs-Ox catalysts as a function of the applied potential is shown in **Figure 3**a. The variation of $\%HO_2^-$ with respect to the fraction of manganese (n) in the catalyst is shown in Figure 3b. The highest $\%HO_2^-$ values (above 35%) were observed in samples where the content of Mn was close or equal to zero, namely, $Fe_{0.3}Ni_{0.7}O_X$ and $Mn_{0.1}(Fe_{0.3}Ni_{0.7})_9O_X$. $\%HO_2^-$ decreased upon increasing the fraction of Mn from 0.1 to 0.5. The best performing sample in terms of selective reduction of O_2 toward OH^- rather than HO_2^- was $Mn_{0.5}(Fe_{0.3}Ni_{0.7})_{0.5}O_X$ with a HO_2^- yield of less than 10%, which is remarkably low for nonprecious catalysts supported on a nitrogen-free carbon material.[14] A further increase in Mn, however, resulted in an increase of the $\%HO_2^-$ yield, reaching values close to 20% when $n = 0.8$. As shown in Figure 3b, the described trend was the same at applied potentials of 0.5, 0.6, and 0.7 V versus RHE. Figure S3a,b in the Supporting Information shows $\%HO_2^-$ as a function of the applied potential for the bimetallic Mn_nNi_{1-n} and Mn_nFe_{1-n} systems, respectively. In both cases, the lowest $\%HO_2^-$ values were observed for samples with $n = 0.5$, and were about 20% and 16% for $Mn_{0.5}Ni_{0.5}O_X$ and $Mn_{0.5}Fe_{0.5}O_X$, respectively, at 0.5 V versus RHE.

The structural properties of the prepared samples, including the degree of defectiveness of MWCNTs-Ox, as well as particle size distribution, crystal structure, and chemical state of the metal nanoparticles, were investigated. Figure S4 in the Supporting Information shows Raman spectra recorded for MWCNTs-Ox, the monometallic samples, and $Mn_n(Fe_{0.3}Ni_{0.7})_{1-n}O_X$/MWCNTs-Ox with $n = 0$, 0.2, 0.4, 0.5, 0.6, and 0.8, displaying in all cases the characteristic D and G bands centered at ≈1352 and ≈1589 cm^{-1}, respectively. The ratios between the intensities of the D and G bands (I_D/I_G ratio) were determined for all the samples, obtaining values between 1.36 and 1.46, which, together with the presence of a broad shoulder at the G band, indicates a high proportion of defects in the carbon surface.[30] Nonmodified MWCNTs exhibited an I_D/I_G ratio of 1.40. Since this value is not substantially different than the I_D/I_G ratios observed with the MO_X/MWCNTs-Ox samples, it can be assumed that most surface defects are originated by the introduction of oxygen functionalities.

Figure 4 shows high-resolution transmission electron microscopy (HRTEM) images of $Mn_{0.5}(Fe_{0.3}Ni_{0.7})_{0.5}O_X$ and its components $Fe_{0.3}Ni_{0.7}$, MnO_X, with their corresponding size

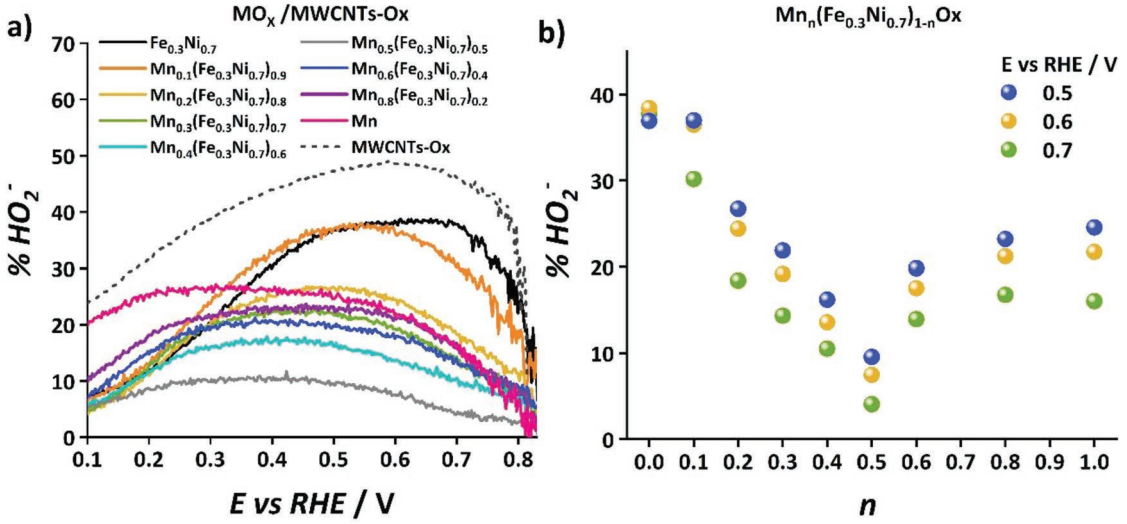

Figure 3. Investigation of the ORR selectivity of $Mn_n(Fe_{0.3}Ni_{0.7})_{1-n}O_X$/MWCNTs-Ox catalysts by rotating ring-disk voltammetry conducted in O_2-saturated 0.1 M KOH, at a scan rate of 5 mV s^{-1}, electrode rotation speed of 1600 rpm, and constant ring electrode potential of 0.4 V versus Ag/AgCl/KCl (3 M). Yield of peroxide species (%HO_2^-) as a function of a) the applied potential, and b) the fraction of Mn (with respect to the total metal content) observed at different electrode potentials.

distributions inside and outside the MWCNTs-Ox. HRTEM analysis of bimetallic $Mn_{0.5}Ni_{0.5}O_X$, $Fe_{0.5}Ni_{0.5}O_X$, and $Mn_{0.5}Fe_{0.5}O_X$ catalysts are shown in Figures S5 in the Supporting Information. For clarity, a summary of the average particle size of relevant samples is shown in Table S5 in the Supporting Information. In agreement with our previous works,[14,15] the average particle size inside the MWCNTs-Ox was defined by the width of the inner diameter of the carbon nanotubes (about 4 nm) and differed from the size of the nanoparticles deposited on the outer walls of MWCNTs-Ox. Previously, we observed that the largest (14.5 nm) and smallest (5.6 nm) nanoparticles were formed by FeO_X and NiO_X, respectively.[15] MnO_X, however, possessed a considerably larger average particle size (36.6 nm) and a wide particle size distribution, ranging from 9.4 to 107.3 nm. Interestingly, the presence of a second metal oxide component led to a decrease of the average particle size to 8.1 and 8.3 nm for $Mn_{0.5}Ni_{0.5}O_X$ and $Mn_{0.5}Fe_{0.5}O_X$, respectively (Figure S5, Supporting Information), suggesting that the combination of MnO_X with a second metal oxide restrains the agglomeration of MnO_X particles. Combining MnO_X with $Fe_{0.3}Ni_{0.7}O_X$ results in a wider particle size distribution than that of $Fe_{0.3}Ni_{0.7}O_X$, but it is substantially narrower than MnO_X with an average of 10.5 nm in the case of a ratio of 1:1 of the two components.

Changes in phase composition and crystal structure of the trimetallic $Mn_n(Fe_{0.3}Ni_{0.7})_{1-n}O_X$/MWCNTs-Ox samples were studied by X-ray diffraction (XRD) in dependence on the composition (**Figure 5**). The reflections at 2θ = 25.9°, 42.9°, and 53.3° were observed in all the samples, and correspond to the MWCNTs. The XRD patterns of the monometallic Mn-containing sample (MnO_X/MWCNTs-Ox) indicate the presence of a tetragonal spinel structure (Mn_3O_4). For this sample, one ensemble of particles with a coherent scattering region (CSR) size of about 20–30 nm was identified. As we reported earlier,[15] for the sample with metal composition $Fe_{0.3}Ni_{0.7}$, a peak was observed at 2θ = 35°–38°, from which the presence of two phases, namely, $FeNi_2O_4$ with a cubic spinel structure and NiO with a NaCl-type structure, can be identified. From the analysis of the peak position (2θ = 35°–38°), it follows that in this case the NiO phase with a NaCl-type structure and a CSR size less than 3 nm was predominant.

The addition of MnO_X to the $Fe_{0.3}Ni_{0.7}O_X$ system led to the appearance of reflections characteristic of phases of highly defective monometallic oxides of iron, manganese, and nickel, as well as their mixed iron-nickel, iron-manganese, and nickel-manganese oxides. For most of the samples, a predominant phase can be distinguished depending on the specific metal composition. However, none of the presented trimetallic samples is monophasic. For all the trimetallic samples, a different content of the NaCl-type phase formed by NiO was observed. With an increase in the manganese content, a decrease in the intensity of the peak (2θ ~ 43.3°) corresponding to the (012) NiO reflection was observed, which indicates a decrease of its relative composition in the sample. The broadening and displacement of the peaks in the 2θ ~ 36.5° and 62.5° regions indicate the presence of Fe_3O_4 and $MnFe_2O_4$ spinels in all the trimetallic samples. The change in the shape and position of the peaks suggests that a particular spinel phase predominates. In samples with a low manganese content (n = 0.1–0.3), the predominance of a highly dispersed and defective NiO phase of the NaCl-type was revealed. At a Mn content of n = 0.4–0.6, a more pronounced broadening of the peaks was observed at 2θ ~ 62.5° and 36.5°, which is most clearly seen for the sample with a Mn content of n = 0.5. Presumably, given the stoichiometric ratios of the components in the samples, all phases were simultaneously present (monometallic iron, manganese and nickel oxides, as well as their mixed iron-nickel, iron-manganese, and nickel-manganese oxides) in a highly defective state. In this case, the formation of a defective crystal lattice formed simultaneously by all the metals, or a set of defective lattices for each of the present phases is possible. In samples with a

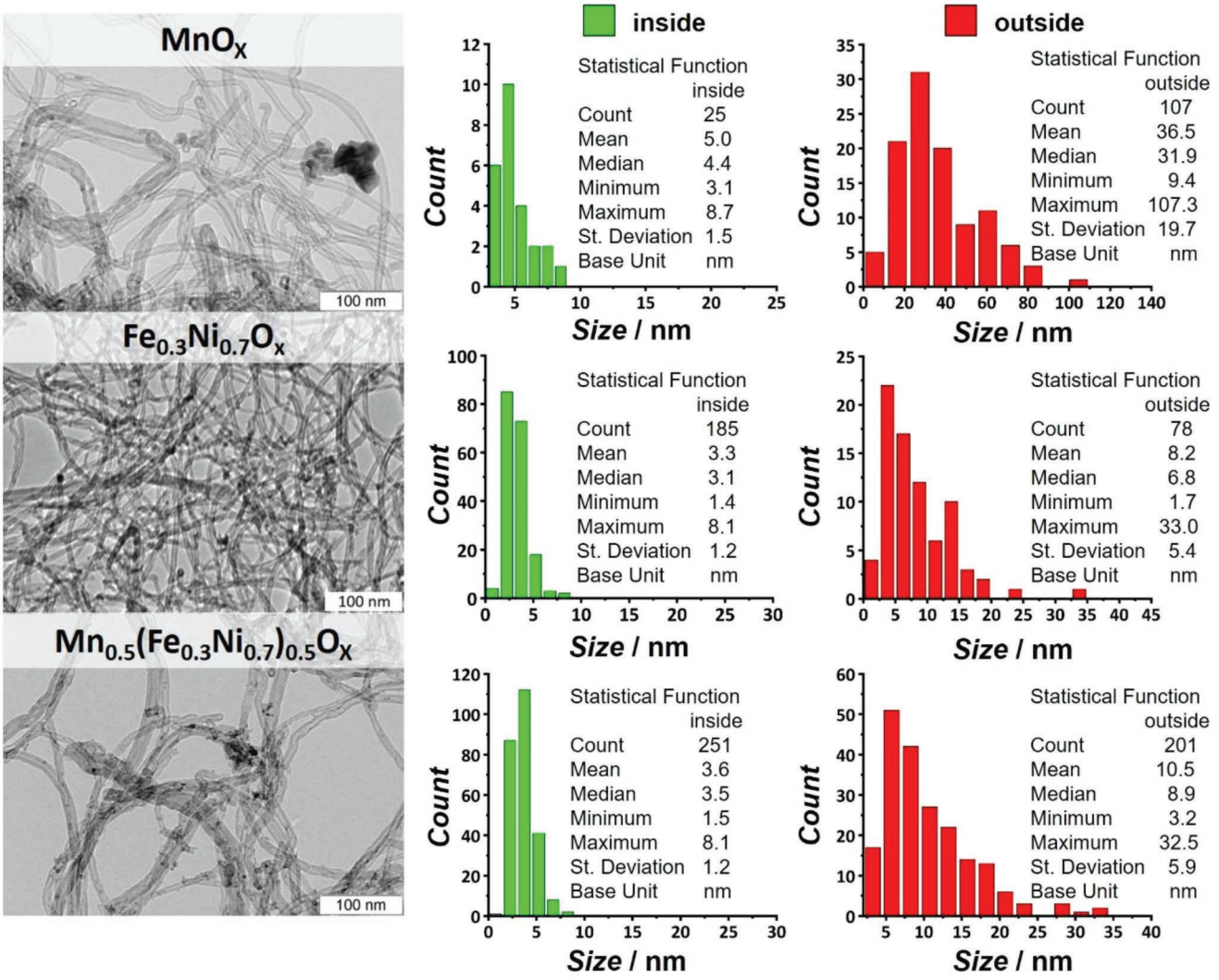

Figure 4. Left: HRTEM images of MO_X nanoparticles with metal composition $Fe_{0.3}Ni_{0.7}$, $Mn_{0.5}(Fe_{0.3}Ni_{0.7})_{0.5}$, and Mn_1, and Right: their corresponding particle size histograms showing the particle size distribution inside (green) and outside (red) the oxidized MWCNTs.

higher content of manganese (n = 0.8), the low crystallized Mn_3O_4 phase with the tetragonal spinel structure prevailed. For a series of trimetallic samples with a manganese content n = 0.1–0.6, one ensemble of particles with a CSR size of less than 3 nm was observed. Increase of the manganese content to 0.8 led to the growth of the CSR size to 5 nm.

The XRD patterns of mono- and bimetallic samples are shown in Figure S6 in the Supporting Information. In agreement with our previous results,[14,15] the monometallic oxides formed Fe_3O_4 and NiO as the main phases. An increase in manganese content in the bimetallic Mn-Ni samples led to a shift of the 2θ peak at ≈37.3° toward smaller values, which suggests a transition from the NiO phase to the mixed manganese-nickel oxide ($Mn_xNi_{1-x}O$) phase.[25,31] For the series of the bimetallic Mn-Ni samples, one ensemble of particles with a CSR size less than 3 nm was observed, regardless of the manganese content (n = 0.3–0.7) in the sample. An increase in the manganese content in the bimetallic Mn-Fe samples from 0.3 to 0.7 led to a shift in the peak position at 2θ = 35°–37°, which indicates a transition from $MnFe_2O_4$ spinel to tetragonal Mn_3O_4. In the sample with manganese content n = 0.3, the $MnFe_2O_4$ phase prevailed, whereas at n = 0.5, the appearance of reflections of the corresponding tetragonal spinel Mn_3O_4 was observed. In the n = 0.7 sample, the Mn_3O_4 phase prevailed. For the series of the bimetallic Mn-Fe samples, one ensemble of particles was observed. The CSR size for samples $Mn_{0.3}Fe_{0.7}$ and $Mn_{0.5}Fe_{0.5}$ was less than 3 nm. An increase in the content of manganese led to an increase in the size of the CSR, with a value of 15 nm being observed for the $Mn_{0.7}Fe_{0.3}$ sample.

The chemical state of the surface of the prepared materials was investigated by high-resolution X-ray photoelectron spectroscopy (XPS). Spectra corresponding to the Ni 2p, Fe 2p, Mn 2p, and Mn 2s core-level regions are shown in **Figure 6**. Despite the low concentration of the metal species, which led to low intensity signals, we were able to confirm the presence of the different metals in an oxidized state at the surface of the different catalysts. All Ni-containing samples displayed the Ni $2p_{3/2}$ peak at ≈855 eV, and a satellite feature at ≈861 eV, which

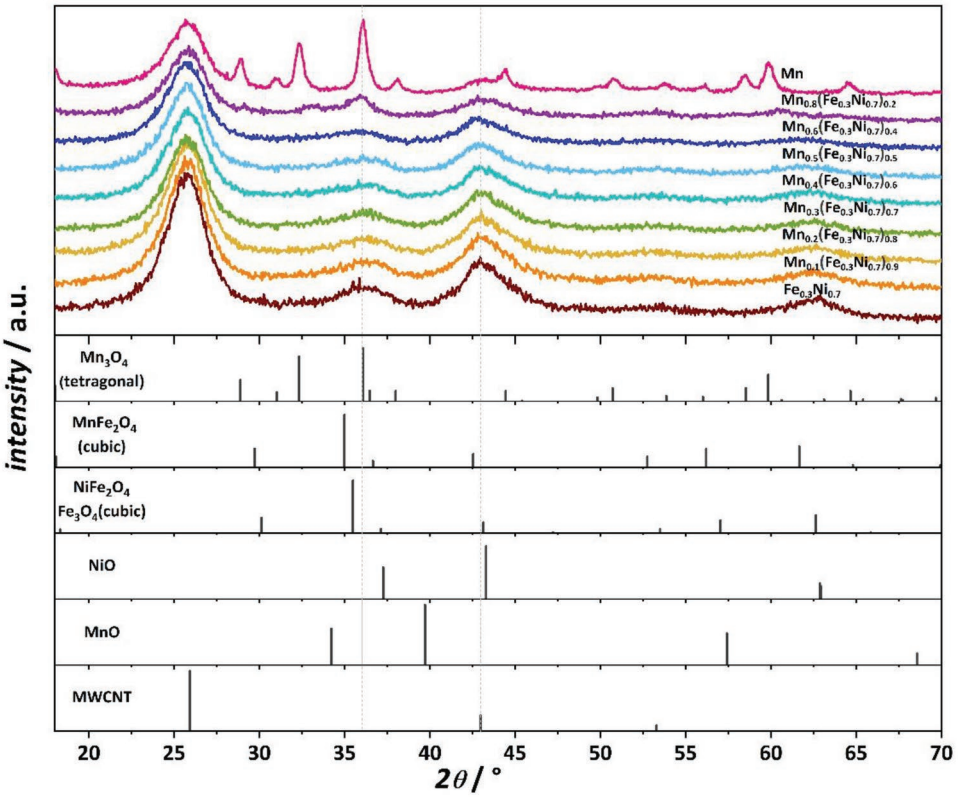

Figure 5. XRD patterns of $Mn_n(Fe_{0.3}Ni_{0.7})_{1-n}O_X$/MWCNTs-Ox catalysts with $n = 0$–1.

corresponds to Ni^{2+} species, such as $Ni(OH)_2$ and $NiFe_2O_4$.[32,33] To further confirm the presence of Ni^{2+}, the XPS signals of $Mn_n(Fe_{0.3}Ni_{0.7})_{1-n}O_X$/MWCNTs-Ox in the Ni 2p region were deconvoluted (Figure S7, Supporting Information). The obtained spectrum is in good agreement with fitted spectra of $Ni(OH)_2$ reported in the literature,[33] suggesting that these are the dominant surface species. In the case of the iron-containing samples, the Fe $2p_{3/2}$ peak was found at ≈711 eV, suggesting that Fe species are present in the 3+ oxidation state.[34] The low content of iron complicates the assessment of both the position of the $2p_{1/2}$ peak and the observation of shake up satellites. However, since the main phases observed by XRD were $NiFe_2O_4$ and $MnFe_2O_4$ in the cases of the iron-rich samples, it is expected that the dominant oxidation state of iron species is 3+. Spinel-type manganese oxides, namely, Mn_3O_4 and $MnFe_2O_4$, were formed in the samples containing manganese, according to XRD analysis. Thus, it was expected that manganese species are present in both the 2+ and 3+ oxidation states. XPS spectra recorded in the Mn 2p core-level region display the Mn $2p_{1/2}$ and $2p_{3/2}$ peaks at ≈653 and ≈642 eV, respectively, indicating that Mn is indeed in an oxidized state.[32] To distinguish between the oxidation states, XPS spectra in the Mn 3s region were recorded. A peak splitting of 5.7 eV was observed, which falls in between the characteristic peak splitting values of Mn^{2+} and Mn^{3+},[35] thus confirming the presence of the two oxidation states. Spectra corresponding to the C 1s and O 1s core-level regions of selected samples are shown in Figure S8 in the Supporting Information. The spectra obtained are consistent with our previous reports,[14,15] showing, on the one hand, the presence of oxidized carbon species in the case of C 1s, and, on the other hand, the peaks corresponding to C-O and C=O in the O 1s region centered at 531.5 and 533.4 eV, respectively,[36] as well as the peak near ≈530 eV ascribed to lattice oxygen in the metal oxides.[32]

Synergistic effects, here understood as the enhancement of electrocatalytic properties of a material resulting from the interaction between two or more different metal components, are a topic of ongoing debate. The origin of these synergies could be related to the influence of the combination of metal sites on the adsorption energies of the chemical species involved in the electrochemical process, thus influencing the coverage and the reaction rate-limiting step,[22] meanwhile the improvement of electrical conductivity[37,38] and the formation of more stable active sites[37] could also play an important role. Even though the underlying mechanism causing the observed synergistic interactions is still under debate, they may be advantageously exploited for the fabrication of highly active catalyst materials. In the case of $Mn_n(Fe_{0.3}Ni_{0.7})_{1-n}O_X$/MWCNTs-Ox, the diversity of highly defective phases together with the narrow distribution of particle sizes achieved only upon combining the different transition metals could also contribute to the observed enhancement of activity (Figure 2) and selectivity (Figure 3). To investigate the surface effects, the double layer capacitance (C_{DL}), which is related to the electrochemically active surface area, was determined for all three monometallic samples, as well as for the bimetallic and trimetallic catalysts which displayed the highest bifunctional ORR/OER activities within their corresponding sets of samples (Table S6, Supporting

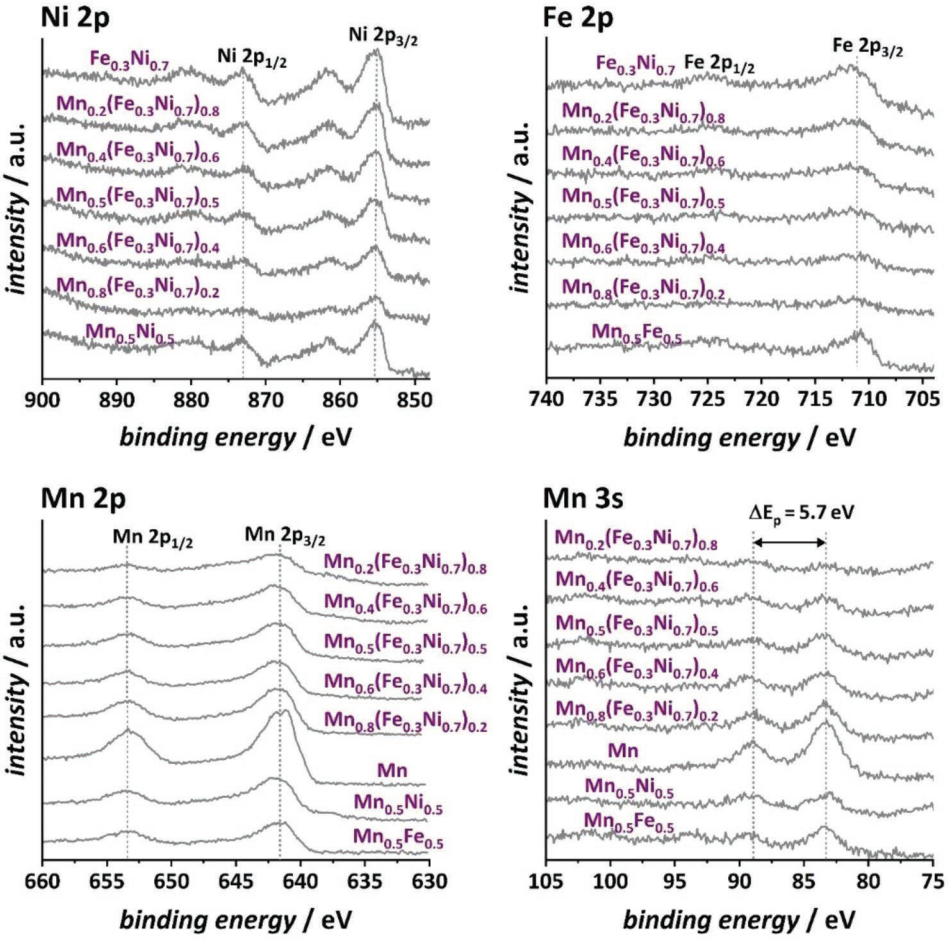

Figure 6. High-resolution XPS spectra of MO_X/MWCNTs-Ox catalysts in the Ni 2p, Fe 2p, Mn 2p, and Mn 3s regions.

Information). As shown in Figure S9 in the Supporting Information, the materials with metal compositions $Mn_{0.5}Ni_{0.5}$, $Mn_{0.5}Fe_{0.5}$, and $Mn_{0.5}(Fe_{0.3}Ni_{0.7})_{0.5}$ displayed the highest C_{DL} values (0.82–0.86 mF), whereas Fe and $Fe_{0.3}Ni_{0.7}$ exhibited the lowest capacitances (0.53–0.57 mF). These values, however, do not correlate with the observed ORR/OER activities, suggesting that the activity enhancement does not originate from surface effects. Galvanostatic EIS under ORR (–1 mA cm^{-2}) and OER (+1 mA cm^{-2}) conditions was conducted to compare qualitatively the charge transfer resistance (R_{ct}) of the different MnO_X/MWCNTs-Ox catalysts. The obtained Nyquist plots are shown in Figure S10 in the Supporting Information. In the case of the ORR, $Mn_{0.5}Ni_{0.5}$ and $Mn_{0.5}(Fe_{0.3}Ni_{0.7})_{0.5}$ exhibited the lowest R_{ct}, whereas in the case of the OER, the lowest R_{ct} were observed with $Mn_{0.5}(Fe_{0.3}Ni_{0.7})_{0.5}$ and $Fe_{0.3}Ni_{0.7}$. The fact that these pairs of samples exhibited the highest activities for the ORR and the OER, respectively, indicates a correlation between R_{ct} and activity, which can be attributed to the difference in reaction kinetics and electrical conductivity between the different samples. Thus, we propose that the enhancement in activity of the catalysts originates from the combination of different metal oxide phases, which, on the one hand, provide the material with a diversity of active sites, and, on the other hand, may induce electronic effects that favor the adsorption energies of the reaction intermediates and the intrinsic catalytic capabilities of the composite (faster kinetics), with an additional improvement of the electrical conductivity.

As stated before, the trimetallic $Mn_n(Fe_{0.3}Ni_{0.7})_{1-n}O_X$/MWCNTs-Ox systems with n = 0.2–0.8 exhibited remarkable bifunctional ORR/OER activity. The low ΔE value observed with $Mn_{0.5}(Fe_{0.3}Ni_{0.7})_{0.5}O_X$/MWCNTs-Ox makes it a promising candidate as electrode material for reversible oxygen electrodes in energy conversion devices, such as reversible electrolyzers/fuel cells and rechargeable metal–air batteries. To evaluate the applicability of this catalyst as such, stability tests were conducted using a chronopotentiometric protocol consisting of, firstly, applying a constant current density of –1 mA cm^{-2} (ORR) for 2 min, and subsequently +10 mA cm^{-2} (OER) for 2 min, and repeating the sequence for a total of 60 min while monitoring the electrode potential. **Figure 7**a (green) shows the variation of overpotential observed during the ORR and OER as a function of time. For comparison, the same protocol was employed alternating between –1 and 0 mA cm^{-2} (only ORR), and between 0 and +10 mA cm^{-2} (only OER) as shown in Figure 7a (blue and yellow, respectively). Only the data recorded during the last 10 s of each current density step in the sequence are shown to exclude capacitive effects. The initially measured ORR and OER potentials were in good agreement with the values observed

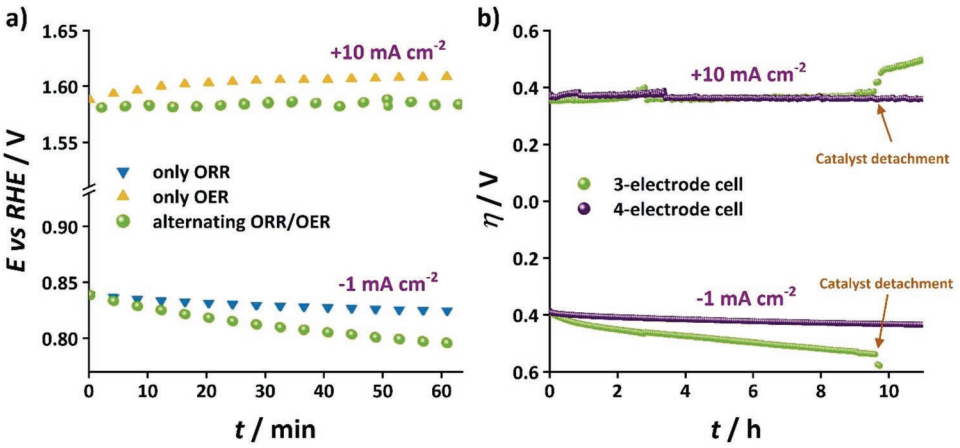

Figure 7. a) Stability of $Mn_{0.5}(Fe_{0.3}Ni_{0.7})_{0.5}O_X$/MWCNTs-Ox determined chronopotentiometrically by alternating either between −1 and 0 mA cm^{-2} (blue), between 0 and +10 mA cm^{-2} (yellow), or between −1 and +10 mA cm^{-2} (green), in 2 min intervals for a total of 60 min. Potentials measured at 0 mA cm^{-2} are not shown. b) Bifunctional ORR/OER stability of $Mn_{0.5}(Fe_{0.3}Ni_{0.7})_{0.5}O_X$/MWCNTs-Ox determined chronopotentiometrically by alternating between −1 and +10 mA cm^{-2} using a three-electrode (green), and a four-electrode (wine) configuration cell. For the latter, the currents corresponding to the ORR and the OER were applied to two independent working electrodes using a two-way relay switch. All measurements were conducted in O_2-saturated 0.1 M KOH maintaining an electrode rotation of 1600 rpm.

from activity tests (E_{ORR} = 0.84 V and E_{OER} = 1.57 V, respectively) for both the bifunctional ORR/OER, and the independent ORR and OER stability tests. The ORR overpotential increased severely over time in the case of the bifunctional ORR/OER stability test, whereas the catalyst exhibited a considerably more stable behavior during the test corresponding only to ORR, suggesting that the deactivation observed in the first case is due to irreversible oxidation of the ORR active sites during OER. In the case of the OER, differences between the observed OER potentials can be ascribed to partial blockage of the electrode surface due to gas bubble formation.[38]

The severe ORR activity loss indicates a poor ORR/OER reversibility of the catalyst, which would evidently impede its use as a single catalytic film for the two reactions. To prevent irreversible oxidation of the ORR active sites during OER, we used a four-electrode cell integrating two equally catalyst-modified working electrodes into a single device by using a relay switch (Figure S11, Supporting Information). By this means, the ORR and the OER take place at two independent electrodes, allowing the use of $Mn_{0.5}(Fe_{0.3}Ni_{0.7})_{0.5}O_X$/MWCNTs-Ox as catalyst in a two-layer reversible ORR/OER system without exposing the individual catalyst films to both reactions. The stability test was repeated and extended for a total of 10 h using both the three- and the four-electrode configuration setups for comparison. As shown in Figure 7b (wine), the increase of ORR overpotentials observed for $Mn_{0.5}(Fe_{0.3}Ni_{0.7})_{0.5}O_X$/MWCNTs-Ox was drastically reduced, and comparatively more stable responses were obtained for both electrodes, thereby demonstrating the applicability of this highly active material for fabrication of OER and ORR catalyst films in a two-layer bifunctional oxygen electrode.

To shed light on the stability of the catalyst with respect to the morphology and composition of the transition metals, scanning electron microscopy/energy dispersive X-ray spectroscopy (SEM/EDX) investigations were performed on the catalyst before and after the bifunctional ORR/OER stability studies for 10 h and representative results are presented in Figures S12 and S13 in the Supporting Information. No obvious changes in the morphology could be discerned from the SEM images owing to the very small sizes of the transition metal catalyst particles. The composition (wt%) of the transition metals in the catalysts from the EDX analysis of Fe (1.82%), Ni (4.63%), and Mn (7.18%) was found in agreement with the nominal loading of the metals before the stability tests (2.1%, 5.0%, 7.3%, respectively), as determined by XRF analysis (Table S1, Supporting Information). After the stability test for 10 h, the composition of the transition metal elements was 1.98, 4.50, and 6.34 wt% for Fe, Ni, and Mn, respectively. Evidently, one may claim a minor decrease of the Mn content, whereas the composition of Ni and Fe was essentially unchanged from the nominal values in the pristine catalyst. However, the observed discrepancies are all within the experimental error of the EDX technique preventing to make firm conclusions on the stability of the catalysts based exclusively on the SEM and EDX results.

3. Conclusion

MnO_X was incorporated into a highly active OER catalyst, consisting of mixed Fe-Ni oxide nanoparticles supported on oxidized MWCNTs, as a design strategy for the activation of the catalyst toward the ORR, and thus, the fabrication of bifunctional oxygen electrodes. It was shown that the combination of the two components influenced structural properties, such as particle size and crystal structure, as well as catalytic properties, including not only the ORR and OER activity, but also the ORR selectivity. The obtained trimetallic composites exhibited notably low ORR/OER overpotentials with a remarkably low ΔE value of only 0.73 V in the case of $Mn_{0.5}(Fe_{0.3}Ni_{0.7})_{0.5}O_X$/MWCNTs-Ox systems. Additionally, the catalyst demonstrated a favorable selectivity toward the reduction of O_2 to OH^- via the four-electron transfer pathway, with a yield of peroxide species

of less than 10%. Finally, by integrating $Mn_{0.5}(Fe_{0.3}Ni_{0.7})_{0.5}O_X$/MWCNTs-Ox into a four-electrode configuration cell, the applicability of the material for reversible ORR/OER applications was demonstrated.

4. Experimental Section

Synthesis of MO_X/MWCNTs-Ox Catalysts: MWCNTs were grown according to a previously reported procedure consisting of chemical vapor deposition of ethylene at 680 °C for 15 min using a FeCo catalyst,[39] followed by a 2 h treatment in boiling hydrochloric acid solution (15 vol%) to remove the catalyst residues.[14] The obtained MWCNTs were washed with distilled water until a neutral pH was obtained. Oxygen functionalities were introduced by treating the obtained samples in concentrated HNO_3 aqueous solution (68 vol%) for 2 h at 120 °C in a reflux condenser. The material was subsequently washed and dried to obtain oxygen functionalized MWCNTs (MWCNTs-Ox)[40] with a purity higher than 99%, being catalyst residues encapsulated inside the tube core the main impurities.[41]

MWCNTs-Ox were modified with oxides of manganese, nickel, and iron via incipient wet impregnation, using aqueous $Mn(NO_3)_2$, $Ni(NO_3)_2$, and $Fe(NO_3)_3$ solutions as precursors. After impregnation, the samples were dried at 110 °C for 4 h. Subsequent annealing at 350 °C for 4 h under an Ar atmosphere yielded the corresponding MO_X/MWCNTs-Ox-type catalysts, where M denotes the nominal metal composition of the samples. The concentrations of the solutions used for impregnation were adjusted to obtain three sets of samples with different metal compositions and ratios, namely, Mn_nFe_{1-n} (n = 0, 0.3, 0.5, 0.7, 1), Mn_nNi_{1-n} (n = 0, 0.3, 0.5, 0.7, 1), and $Mn_n(Fe_{0.3}Ni_{0.7})_{1-n}$ (n = 0.1, 0.2, 0.3, 0.4, 0.5, 0.6, 0.8), for a total metal loading between 13.5 and 14.5 wt%.

Structural Characterization: XRF was used for elemental analysis using an ARL Perform'X spectrometer (Thermo Fischer Scientific) equipped with a Rh anode X-ray tube. Prior to the measurement, the samples were grounded in an agate mortar and mixed with cellulose at a weight ratio of 1:5, pressed into a tablet, and placed in the sample holder for analysis. Five scans were collected, and the program UniQuant was used for assessing the metal content in each of the prepared samples.

Raman spectra were obtained using a Jubin-Yvon iHR550 spectrometer (HORIBA) equipped with a laser source of λ = 532 nm (Ventus 532, Laser Quantum). The measurements were conducted using a laser power of 2 mW, a grating of 1200 grooves mm^{-1}, and a 60x magnification objective.

N_2 adsorption isotherms were obtained on an ASAP-2400 instrument (Micromeritics) at a temperature of 77 K for the determination of specific surface areas.

The microstructure of the prepared materials was analyzed by HRTEM, using a JEM-2010 microscope (JEOL). The samples were dispersed in dimethylformamide,[42] drop cast onto a micromesh copper grid and transferred to the vacuum chamber where the solvent was evaporated. The microscope was operated at an accelerating voltage of 200 kV (nominal resolution 1.4 Å). The software package Gatan Micrograph was used for statistical analysis of 200–300 tubes, which enabled determination of the average inner and outer diameter of the MWCNTs and the particle size distribution of the metal oxide nanoparticles.

XRD was used for the determination of the metal oxide phases in the different samples. XRD measurements were conducted with an ARL X'TRA diffractometer (Thermo Electron Corporation) equipped with vertical theta geometry (Bragg-Brentano), a Cu K_α X-ray source (λ = 0.15418 nm), and a Peltier-cooled Si (Li) solid-state X-ray detector. The data were collected in the 2θ range from 18° to 70° in 0.05° steps and 3 s counting time. Phase identification and phase composition were assessed with the ICDD PDF-2 database and Rietveld analysis, respectively, using the software Topas.

XPS was carried out with an AXIS Nova spectrometer (Kratos Analytical) equipped with a monochromatic Al K_α X-ray source (1487 eV, 15 mA emission current), maintaining a chamber pressure of $\approx 2 \times 10^{-9}$ mbar. The high-resolution spectra of the core levels were collected in the fixed transmission mode at a pass energy of 20 eV. Charging effects were compensated using a flood gun during spectra acquisition. The main C 1s sp^2 peak at 284.5 eV was used for calibration of the binding energies.

SEM and EDX analyses were performed with a Quanta 3D FEG microscope (FEG). The investigated sample was dispersed in a mixture of water and ethanol (1:1 volume ratio) and drop cast onto an aluminum foil.

Electrochemical Characterization: Electrochemical measurements were performed in a three-electrode cell configuration using an Autolab PGSTAT bipotentiostat/galvanostat (Metrohm) to control the electrode potentials. Catalyst inks were prepared by dispersing 5 mg mL^{-1} catalyst powder in a mixture of ultrapure water, ethanol, and Nafion solution in the volume ratio of 49:49:2, with the aid of sonication for 15 min. Pre-polished rotating disk electrodes (RDEs, glassy carbon, 0.113 cm^2 geometric area) and RRDEs (glassy carbon disk and platinum ring of 0.196 and 0.153 cm^2 geometric area, respectively), were modified by drop casting 210 µg cm^{-2} catalyst ink onto the glassy carbon disk, and were left to dry under air for 30 min. The modified electrodes, a platinum mesh, and a Ag/AgCl/KCl (3 M) electrode were used as the working, the counter, and the reference electrode, respectively. The counter electrode was kept in a compartment separated by means of a glass frit during the measurements to avoid contamination of the working electrode with potentially dissolved Pt. A 0.1 M KOH solution was used as electrolyte. Prior to each electrochemical experiment, the electrolyte was purged with oxygen for 15 min. An oxygen stream was kept near the surface of the solution during the measurements. Electrochemical impedance spectra were collected at open-circuit potential (OCP) in the frequency range from 50 kHz to 10 Hz with a 10 mV AC amplitude to determine the solution resistance (R_s). Subsequently, continuous cyclic voltammograms were collected in the potential range from 0.4 to −0.5 V versus Ag/AgCl/KCl (3 M) at a scan rate of 100 mV s^{-1} until a reproducible response was obtained.

The ORR/OER activity and ORR selectivity of the samples were evaluated by RDE and RRDE voltammetry, respectively. Linear sweep voltammograms were recorded in the potential range from 0.2 to −1 V versus Ag/AgCl/KCl (3 M), and from 0.1 to 0.9 V versus Ag/AgCl/KCl (3 M) for the ORR and OER, respectively, with a scan rate of 5 mV s^{-1} and a rotation speed of 1600 rpm. All activity measurements were carried out in triplicate and the reported data correspond to the average of the three independent measurements. For the ORR selectivity measurements, linear sweep voltammograms were recorded at the disk electrode in the potential range from 0.2 to −1 V versus Ag/AgCl/KCl (3 M) at a scan rate of 5 mV s^{-1} and an electrode rotation of 1600 rpm, while a potential of 0.4 V versus Ag/AgCl/KCl (3 M) was maintained at the ring electrode. The percentage of peroxide species produced ($\%HO_2^-$) was calculated from the background-corrected disk (i_{disk}) and ring (i_{ring}) currents, and the collection efficiency factor (N), according to Equation (1). A 5×10^{-3} M potassium hexacyanoferrate solution dissolved in Ar-saturated 0.1 M KOH was used for determining N for each investigated catalyst film[43]

$$\%HO_2^- = 200 * \frac{\left(\frac{i_{ring}}{N}\right)}{\left(\frac{i_{ring}}{N}\right) + i_{disk}} \quad (1)$$

Double layer capacitance (C_{DL}) was determined by cyclic voltammetry recorded in the non-Faradaic potential region[43] at scan rates of 0.005, 0.01, 0.05, 0.1, and 0.2 V s^{-1}. The charging currents measured at OCP were plotted as a function of the scan rate, and the slopes resulting from the linear fit were extracted and reported as C_{DL}. Galvanostatic electrochemical impedance spectra were recorded in the frequency region from 50 kHz to 0.01 Hz with a perturbation current of 50 µA (RMS) and constant current densities of −1 and +10 mA cm^{-2}

to determine the charge transfer resistance during ORR and OER, respectively.

A chronopotentiometric protocol with alternating ORR (–1 mA cm^{-2}) and OER (+10 mA cm^{-2}) current steps of 2 min each was applied for a total duration of 10 h. Constant electrode rotation at 1600 rpm was maintained to facilitate gas bubble departure from the catalyst film. For comparison, the protocol was repeated alternating between ORR (–1 mA cm^{-2}) and 0 mA cm^{-2}, and between 0 mA cm^{-2} and OER (+10 mA cm^{-2}) for 1 h. The stability test protocol employed in the three-electrode cell setup was further conducted in a four-electrode cell configuration where two working electrodes were used, one exclusively for the ORR and the other for the OER, by employing a two-way relay switch to alternate between the two electrodes. Before switching, each electrode was maintained at 0 A for 30 s.

All measured potentials were iR-drop compensated and converted to the RHE scale according to Equation (2)

$$E_{RHE} = E_{Ag/AgCl/KCl} + 0.059\,pH + 0.207 - iR_s \quad (2)$$

The pH of the solution was determined with a CP-411 pH-meter (Elmetron).

Supporting Information

Supporting Information is available from the Wiley Online Library or from the author.

Acknowledgements

D.M.M. and M.A.K. contributed equally to this work. The authors are grateful to the Bundesministerium für Bildung und Forschung (BMBF) in the frameworks of the project "Mangan" (FKZ 03EK3548). D.M.M. acknowledges the financial support from Deutscher Akademischer Austauschdienst (DAAD) and from Consejo Nacional de Ciencia y Tecnología (CONACyT). M.A.K. is grateful to the Russian Foundation for Basic Research, which funded this study via grant 16-32-60046 mol_a_dk. The Boreskov Institute of Catalysis team acknowledges financial support by the Ministry of Science and Higher Education of the Russian Federation (Project AAAA-A17-117041710085-9). S.D. gratefully acknowledges financial support by the International Max-Planck Research School on Reactive Structure Analysis for Chemical Reactions (IMPRS-RECHARGE). The authors are grateful to Dr. Thomas Erichsen and João R. C. Junqueira for their support with the setup for stability tests.

Conflict of Interest

The authors declare no conflict of interest.

Keywords

bifunctional electrocatalysts, oxidized multi-walled carbon nanotubes, oxygen evolution reaction, oxygen reduction reaction, synergistic effects

Received: July 23, 2019
Revised: October 17, 2019
Published online: November 14, 2019

[1] a) M. Tahir, L. Pan, F. Idrees, X. Zhang, L. Wang, J.-J. Zou, Z. L. Wang, *Nano Energy* **2017**, *37*, 136; b) F. M. Sapountzi, J. M. Gracia, C. J. Weststrate, H. O. A. Fredriksson, J. W. Niemantsverdriet, *Prog. Energy Combust. Sci.* **2017**, *58*, 1.
[2] Y. Wang, J. Li, Z. Wei, *J. Mater. Chem. A* **2018**, *6*, 8194.
[3] F. Song, L. Bai, A. Moysiadou, S. Lee, C. Hu, L. Liardet, X. Hu, *J. Am. Chem. Soc.* **2018**, *140*, 7748.
[4] Y. Matsumoto, E. Sato, *Mater. Chem. Phys.* **1986**, *14*, 397.
[5] Y. Jiao, Y. Zheng, M. Jaroniec, S. Z. Qiao, *Chem. Soc. Rev.* **2015**, *44*, 2060.
[6] T. Zhang, Y. Zhu, J. Y. Lee, *J. Mater. Chem. A* **2018**, *6*, 8147.
[7] T. Li, Y. Lv, J. Su, Y. Wang, Q. Yang, Y. Zhang, J. Zhou, L. Xu, D. Sun, Y. Tang, *Adv. Sci.* **2017**, *4*, 1700226.
[8] a) C. Broicher, J. Artz, S. Palkovits, H. Antoni, M. Drögeler, D. M. Morales, C. Stampfer, R. Palkovits, *Catal. Sci. Technol.* **2018**, *8*, 1517; b) Y. Qiu, L. Xin, W. Li, *Langmuir* **2014**, *30*, 7893.
[9] a) J. Du, F. Cheng, S. Wang, T. Zhang, J. Chen, *Sci. Rep.* **2015**, *4*, 4386; b) K. Kaare, I. Kruusenberg, M. Merisalu, L. Matisen, V. Sammelselg, K. Tammeveski, *J. Solid State Electrochem.* **2016**, *20*, 921; c) I. Kruusenberg, L. Matisen, Q. Shah, A. M. Kannan, K. Tammeveski, *Int. J. Hydrogen Energy* **2012**, *37*, 4406.
[10] J. Masa, W. Xia, I. Sinev, A. Zhao, Z. Sun, S. Grützke, P. Weide, M. Muhler, W. Schuhmann, *Angew. Chem., Int. Ed.* **2014**, *53*, 8508.
[11] Y. Zhao, K. Kamiya, K. Hashimoto, S. Nakanishi, *J. Phys. Chem. C* **2015**, *119*, 2583.
[12] S. N. Faisal, E. Haque, N. Noorbehesht, H. Liu, M. M. Islam, L. Shabnam, A. K. Roy, E. Pourazadi, M. S. Islam, A. T. Harris, A. I. Minett, *Sustainable Energy Fuels* **2018**, *2*, 2081.
[13] a) F. Cheng, J. Chen, *Chem. Soc. Rev.* **2012**, *41*, 2172; b) H. Dau, C. Limberg, T. Reier, M. Risch, S. Roggan, P. Strasser, *ChemCatChem* **2010**, *2*, 724.
[14] K. Elumeeva, M. A. Kazakova, D. M. Morales, D. Medina, A. Selyutin, G. Golubtsov, Y. Ivanov, V. Kuznetzov, A. Chuvilin, H. Antoni, M. Muhler, W. Schuhmann, J. Masa, *ChemSusChem* **2018**, *11*, 1204.
[15] M. A. Kazakova, D. M. Morales, C. Andronescu, K. Elumeeva, A. G. Selyutin, A. V. Ishchenko, G. V. Golubtsov, S. Dieckhöfer, W. Schuhmann, J. Masa, *Catal. Today* **2019**, https://doi.org/10.1016/j.cattod.2019.02.047.
[16] R. A. Rincon, J. Masa, S. Mehrpour, F. Tietz, W. Schuhmann, *Chem. Commun.* **2014**, *50*, 14760.
[17] H. Zhong, R. Tian, X. Gong, D. Li, P. Tang, N. Alonso-Vante, Y. Feng, *J. Power Sources* **2017**, *361*, 21.
[18] D. M. Morales, J. Masa, C. Andronescu, Y. U. Kayran, Z. Sun, W. Schuhmann, *Electrochim. Acta* **2016**, *222*, 1191.
[19] K. A. Stoerzinger, M. Risch, B. Han, Y. Shao-Horn, *ACS Catal.* **2015**, *5*, 6021.
[20] A. Paulraj, Y. Kiros, M. Göthelid, M. Johansson, *Catalysts* **2018**, *8*, 328.
[21] G. Liu, D. He, R. Yao, Y. Zhao, J. Li, *Nano Res.* **2018**, *11*, 1664.
[22] O. Diaz-Morales, I. Ledezma-Yanez, M. T. M. Koper, F. Calle-Vallejo, *ACS Catal.* **2015**, *5*, 5380.
[23] Z. Lu, L. Qian, Y. Tian, Y. Li, X. Sun, X. Duan, *Chem. Commun.* **2016**, *52*, 908.
[24] Z.-F. Huang, J. Wang, Y. Peng, C.-Y. Jung, A. Fisher, X. Wang, *Adv. Energy Mater.* **2017**, *7*, 1700544.
[25] H. Osgood, S. V. Devaguptapu, H. Xu, J. Cho, G. Wu, *Nano Today* **2016**, *11*, 601.
[26] Y. Liang, Y. Li, H. Wang, J. Zhou, J. Wang, T. Regier, H. Dai, *Nat. Mater.* **2011**, *10*, 780.
[27] M. S. Ahmed, B. Choi, Y.-B. Kim, *Sci. Rep.* **2018**, *8*, 2543.
[28] S. Dresp, F. Luo, R. Schmack, S. Kühl, M. Gliech, P. Strasser, *Energy Environ. Sci.* **2016**, *9*, 2020.
[29] I. M. Mosa, S. Biswas, A. M. El-Sawy, V. Botu, C. Guild, W. Song, R. Ramprasad, J. F. Rusling, S. L. Suib, *J. Mater. Chem. A* **2016**, *4*, 620.
[30] L. T. M. Hoa, *Diamond Relat. Mater.* **2018**, *89*, 43.
[31] A. R. Denton, N. W. Ashcroft, *Phys. Rev. A* **1991**, *43*, 3161.

[32] M. C. Biesinger, B. P. Payne, A. P. Grosvenor, L. W. M. Lau, A. R. Gerson, R. S. C. Smart, *Appl. Surf. Sci.* **2011**, *257*, 2717.
[33] A. P. Grosvenor, M. C. Biesinger, R. S. C. Smart, N. S. McIntyre, *Surf. Sci.* **2006**, *600*, 1771.
[34] A. P. Grosvenor, B. A. Kobe, M. C. Biesinger, N. S. McIntyre, *Surf. Interface Anal.* **2004**, *36*, 1564.
[35] J. C. Carver, G. K. Schweitzer, T. A. Carlson, *J. Chem. Phys.* **1972**, *57*, 973.
[36] S. Kundu, Y. Wang, W. Xia, M. Muhler, *J. Phys. Chem. C* **2008**, *112*, 16869.
[37] D. A. Corrigan, *J. Electrochem. Soc.* **1987**, *134*, 377.
[38] L. Trotochaud, S. L. Young, J. K. Ranney, S. W. Boettcher, *J. Am. Chem. Soc.* **2014**, *136*, 6744.
[39] a) S. N. Bokova-Sirosh, V. L. Kuznetsov, A. I. Romanenko, M. A. Kazakova, D. V. Krasnikov, E. N. Tkachev, Y. I. Yuzyuk, E. D. Obraztsova, *J. Nanophotonics* **2016**, *10*, 012526; b) A. S. Andreev, D. V. Krasnikov, V. I. Zaikovskii, S. V. Cherepanova, M. A. Kazakova, O. B. Lapina, V. L. Kuznetsov, J.-B. d'Espinose de Lacaillerie, *J. Catal.* **2018**, *358*, 62.
[40] M. A. Kazakova, A. S. Andreev, A. G. Selyutin, A. V. Ishchenko, A. V. Shuvaev, V. L. Kuznetsov, O. B. Lapina, J.-B. d'Espinose de Lacaillerie, *Appl. Surf. Sci.* **2018**, *456*, 657.
[41] V. L. Kuznetsov, K. V. Elumeeva, A. V. Ishchenko, N. Y. Beylina, A. A. Stepashkin, S. I. Moseenkov, L. M. Plyasova, I. Y. Molina, A. I. Romanenko, O. B. Anikeeva, E. N. Tkachev, *Phys. Status Solidi B* **2010**, *247*, 2695.
[42] G. M. Mikheev, V. L. Kuznetsov, K. G. Mikheev, T. N. Mogileva, M. A. Shuvaeva, S. I. Moseenkov, *Tech. Phys. Lett.* **2013**, *39*, 337.
[43] C. C. L. McCrory, S. Jung, J. C. Peters, T. F. Jaramillo, *J. Am. Chem. Soc.* **2013**, *135*, 16977.